OPEN

NPG Asia Materials (2016) 8, e272; doi:10.1038/am.2016.61
www.nature.com/am

ORIGINAL ARTICLE

Graphene quantum dots: structural integrity and oxygen functional groups for high sulfur/sulfide utilization in lithium sulfur batteries

Jungjin Park[1,2,13], Joonhee Moon[3,13], Chunjoong Kim[4,13], Jin Hyoun Kang[3], Eunhak Lim[3], Jaesung Park[5], Kyung Jae Lee[1,2], Seung-Ho Yu[1,2], Jung-Hye Seo[6,7], Jouhahn Lee[6], Jiyoung Heo[8], Nobuo Tanaka[9], Sung-Pyo Cho[10], Jeffrey Pyun[11], Jordi Cabana[12], Byung Hee Hong[3] and Yung-Eun Sung[1,2]

Lithium–sulfur (Li–S) batteries are expected to overcome the limit of current energy storage devices by delivering high specific energy with low material cost. However, the potential of Li–S batteries has not yet been realized because of several technical barriers. Poor electrochemical performance is mainly attributed to the low electrical conductivity of the fully charged and discharged species, the irreversible loss of polysulfide anions and the decrease in the number of electrochemically active reaction sites during battery operation. Here, we report that the introduction of graphene quantum dots (GQDs) into the sulfur cathode dramatically enhanced sulfur/sulfide utilization, yielding high performance. In addition, the GQDs induced structural integrity of the sulfur–carbon electrode composite by oxygen-rich functional groups. This hierarchical architecture enabled fast charge transfer while minimizing the loss of lithium polysulfides, which is attributed to the physicochemical properties of GQDs. The mechanisms through which excellent cycling and rate performance are achieved were thoroughly studied by analyzing capacity versus voltage profiles. Furthermore, experimental observations and theoretical calculations further clarified the role played by GQDs by proving that C–S bonding occurs. Thus, the introduction of GQDs into Li–S batteries will provide an important breakthrough allowing their use as high-performance and low-cost batteries for next-generation energy storage systems.
NPG Asia Materials (2016) **8,** e272; doi:10.1038/am.2016.61; published online 20 May 2016

INTRODUCTION

Rechargeable lithium-ion batteries are widely used in various applications, such as portable devices, bio-medical implants and electric vehicles, because of their high energy and power density.[1,2] However, current lithium-ion batteries based on the graphite and transition metal oxide couple have nearly reached their ceiling with respect to storage capability because of the limitations associated with their electrical properties and crystal structure. Therefore, breakthroughs in new energy storage systems that can surpass the current performance barrier of lithium-ion batteries should be brought about in a timely manner. Recently, Li–S batteries that can operate by the reversible electrochemical transformation between sulfur (S_8) and dilithium sulfide (Li_2S) have attracted great attention because they can deliver high energy with a moderate voltage owing to the direct use of elemental lithium and sulfur as an anode and a cathode, respectively.[3] Sulfur generated from petroleum refinement is an ideal choice for a cathode owing to its low cost, environmental friendliness, and high theoretical specific capacity (1675 mAh g^{-1} by 16 electron process) when it is fully reduced to Li_2S.[2–4] However, several barriers limit the efficient use of sulfur as a cathode: the deleterious electrochemically induced volume expansion from S_8 to Li_2S (~80%), the poor electronic conductivities of S_8 ($\sim 1\times10^{-30}$ S m^{-1}) and Li_2S ($\sim 1\times10^{-14}$ S m^{-1}), and the irreversible loss of high-order polysulfides (HOPSs) to the electrolyte.[5,6] In particular, the loss of HOPSs during cycling is responsible for poor cycle stability, low sulfur utilization and the polysulfide-shuttle phenomenon.[3] To overcome this issue, various carbonaceous materials have been integrated into the sulfur cathode matrix to take advantage of their high electronic

[1]School of Chemical and Biological Engineering, Seoul National University, Seoul, Republic of Korea; [2]Center for Nanoparticle Research, Institute for Basic Science, Seoul, Republic of Korea; [3]Department of Chemistry, College of Natural Science, Seoul National University, Seoul, Republic of Korea; [4]School of Materials Science and Engineering, Chungnam National University, Daejeon, Republic of Korea; [5]Korea Research Institute of Standards and Science, Daejeon, Republic of Korea; [6]Korea Basic Science Institute, Daejeon, Republic of Korea; [7]Yonsei Center for Research Facilities, Seoul, Republic of Korea; [8]Department of Biomedical Technology, Sangmyung University, Chungnam, Republic of Korea; [9]EcoTopia Science Institute, Nagoya University, Nagoya, Japan; [10]National Center for Inter-University Research Facilities, Seoul National University 1 Gwank-ro Gwanak-gu, Seoul, Republic of Korea; [11]Department of Chemistry and Biochemistry, University of Arizona, Tucson, AZ, USA and [12]Department of Chemistry, University of Illinois at Chicago, Chicago, IL, USA
[13]These authors contributed equally to this work.
Correspondence: Professor BH Hong, Department of Chemistry, College of Natural Science, Seoul National University, Seoul 151-747, Republic of Korea.
E-mail: byunghee@snu.ac.kr
or Professor Y-E Sung, School of Chemical and Biological Engineering, Seoul National University, Republic of Korea and Center for Nanoparticle Research, Institute for Basic Science, Seoul 151-742, Republic of Korea.
E-mail: ysung@snu.ac.kr
Received 14 December 2015; revised 29 February 2016; accepted 6 March 2016

conductivity as well as their physicochemical properties to prevent HOPS dissolution into the electrolyte.[7–11] Among many carbonaceous materials, graphene oxide–sulfur composites have been intensively reported as a novel material for preventing the loss of HOPSs through the adsorption and wrapping properties of graphene oxide.[12–16] Despite significantly enhancing the electrochemical stability, these systems can be further improved by exhibiting better structural integrity.[17] In previous studies, both the S and graphene oxide used in batteries were reported to measure on the order of several micrometers; thus, conformal contact between graphene oxide and S is difficult to achieve, allowing HOPSs to be lost by repeated electrochemical cycling.

Recently, graphene particles measuring a few nanometers, graphene quantum dots (GQDs), were successfully synthesized; these particles were shown to demonstrate the quantum confinement effect, resulting in tunable electronic and optical properties.[18,19] Interestingly, GQDs are enriched with oxygen functional groups on their edges, whereby unique properties such as a non-zero bandgap and luminescence on excitation have been reported.[20–22] Furthermore, it is expected that GQDs can uniformly cover the target material due to their small size. Indeed, GQDs have been reported to serve as a composite member or coating material for energy storage devices.[23,24]

The current study is the first to introduce a GQDs-sulfur composite in a Li–S battery. Nano-sized GQDs (an average particle size of ~4 nm) enriched in oxygen functional groups could enhance the structural integrity of a conventional micron-sized sulfur–carbon electrode composite, forming a tightly packed structure. This hierarchical architecture facilitated charge conduction while minimizing the irreversible loss of HOPSs, thus enabling high sulfur/sulfide utilization even at a high current density. To study the mechanism through which enhanced electrochemical performance is achieved, careful analyses of capacity versus voltage profiles were carried out. Furthermore, we observed that the oxygen functional groups of GQDs help preserve dissolved HOPSs by the formation of C–S bonds (the so-called sulfiphilic property), as corroborated by various analytical tools and density functional theory (DFT) calculations. We believe that our results provide a new avenue for material scientists to make the best use of oxygen-rich functional groups in nano-sized carbon for various applications.

EXPERIMENTAL PROCEDURES

Synthesis of graphene quantum dots

GQDs were synthesized using a modified Hummer's method. Carbon fibers were placed into a mixture of H_2SO_4 and HNO_3. The solution was sonicated for 2 h and then stirred for 24 h. The solution was subsequently refluxed at 90 °C for 48 h under vigorous stirring. The resultant mixture was cooled to room temperature and diluted with deionized water, and the pH was adjusted to 8 with Na_2CO_3. The final product was dialyzed for 5 days and then filtered. Finally, the aqueous solution of GQDs was concentrated.

Synthesis of GQDs-S/carbon black (CB) composites

In 250 ml deionized water, 1.5 g of sodium thiosulfate ($Na_2S_2O_3$) powder as the precursor (Sigma Aldrich Corp., St Louis, MO, USA) was dissolved and then stirred while adding hydrochloric acid to obtain sulfur powders by chemical reduction. After the precipitation of sulfur, 1.0 vol% of a Triton X-100 aqueous solution (15 ml) and the 80 mg of the synthesized GQDs (4 mg ml^{-1}) were sequentially added into the solution, followed by heating at ~70 °C. The solution was again vigorously stirred for 20 min, whereby a GQDs-S composite could be prepared. A carbon black (CB) suspension was then added to this GQDs-S suspension and was stirred for another 20 min. Then, the solution was cooled to room temperature, and the collected products were rinsed several times using deionized water. Finally, GQDs-S/CB composites could be obtained by drying under vacuum.

Cell fabrication and electrochemical measurements

The electrodes were fabricated from slurries that contained 60 wt% sulfur, 20 wt% CB as a conducting agent and 20 wt% polyvinylidene fluoride binder dispersed in N-methyl-2-pyrrolidone (2 ml). The prepared slurry was cast onto aluminum foil using a doctor blade. The prepared electrodes were transferred to an Ar-filled glove box and were assembled into a 2032-type coin cell. The mass loading of all samples was ~1.0 or ~2.2 mg cm^{-2} of active material. An electrolyte containing 1.0 M LiTFSI (lithium bis-trifluoromethanesulfonimide) and 0.1 M $LiNO_3$ (lithium nitrate) with dioxolane and dimethyl ether in a 1:1 volume ratio (Panax Etec, Busan, Republic of Korea) was prepared and used in each sample at a volume of 40 μl. The polymeric separator used in the samples was supplied by SK Innovation (Republic of Korea), and lithium metal was used as a counter electrode. Electrochemical properties were measured with a WBCS3000 cycler (Won-A Tech, Seoul, Republic of Korea). The voltage window for the electrochemical measurements was set to 1.5–3.0 V versus Li$^+$/Li (all the voltages below are referenced by redox potential of Li, Li$^+$/Li). CB and GQDs/CB (the mixture of CB and GQDs, 1:1 weight ratio) electrodes were fabricated similarly to the aforementioned procedures from slurries that contained 80 wt% CB and GQDs/CB, and 20 wt% polyvinylidene fluoride binder dispersed in N-methyl-2-pyrrolidone (2 ml).

Li_2S_8 catholyte was prepared using Li_2S and S_8 powders (Sigma Aldrich Corp., USA), which were added to 1.0 M LiTFSI (lithium bis-trifluoromethanesulfonimide) and 0.1 M $LiNO_3$ (lithium nitrate) with dioxolane and dimethyl ether in a 1:1 volume ratio (Panax Etec, Republic of Korea). After cycle operation, the coin cells were disassembled in an Ar-filled glove box and thoroughly rinsed with copious amounts of DOL/dimethyl ether before analysis. Electrochemical impedance spectroscopy measurements were performed at an open-circuit potential between 100 and 100 mHz with fluctuations of <10 mV, and the resulting Nyquist plots were fitted based on the equivalent circuits.

Characterization techniques

X-ray diffraction (XRD) was performed on a Smartlab diffractometer (Rigaku) equipped with a rotating anode and a Cu K*a* radiation source (λ_{avg} = 1.5418 Å) at 45 kV and 200 mA. Transmission electron microscopy (TEM) was performed on a JEOL JEM-2100 F (JEOL, Japan). Scanning TEM, energy dispersive X-ray spectroscopy (EDS) and electron energy loss spectroscopy mapping were carried out with a Tecnai F20 (FEI) equipped with an EDAX Tecnai 136-5 detector. Scanning electron microscopy (SEM) was performed using a SUPRA 55VP FE-SEM (Carl Zeiss). X-ray photoelectron spectroscopy (XPS) was performed on an AXIS Ultra DLD (Kratos Inc.) using a 150-W monochromatic Al K*a* (1486.6 eV) X-ray source at the Korea Basic Science Institute. High-resolution XPS data were collected over a pass energy of 40 eV in 0.05 eV steps. XPS data were fitted using XPS Peak41 software. Raman spectra were obtained using a micro-Raman spectrometer (Renishaw) with an excitation wavelength of 514.5 nm. The diameter of the beam spot was ~1 μm. Fourier transform infrared spectra were obtained by a Nicolet 6700 (Thermo Scientific, Waltham, MA, USA).

Computational methods

DFT calculations were carried out to optimize structures and analyze frequencies. The conventional B3LYP exchange-correlation functional was used for the DFT calculations. B3LYP is a hybrid-GGA exchange-correlation functional, which means the size-consistency problem cannot be considered.[25] To more precisely describe the anion systems, we used a 6-31++G(d) basis set, which added diffuse functions to all atoms. All structures reported in this paper were optimized, as confirmed by frequency analysis. The GAUSSIAN 09 package was used for all calculations.[26]

RESULTS AND DISCUSSION

Material characterization

Characterization of GQDs. Various microscopic and spectroscopic analytical tools were employed to study the physical/chemical

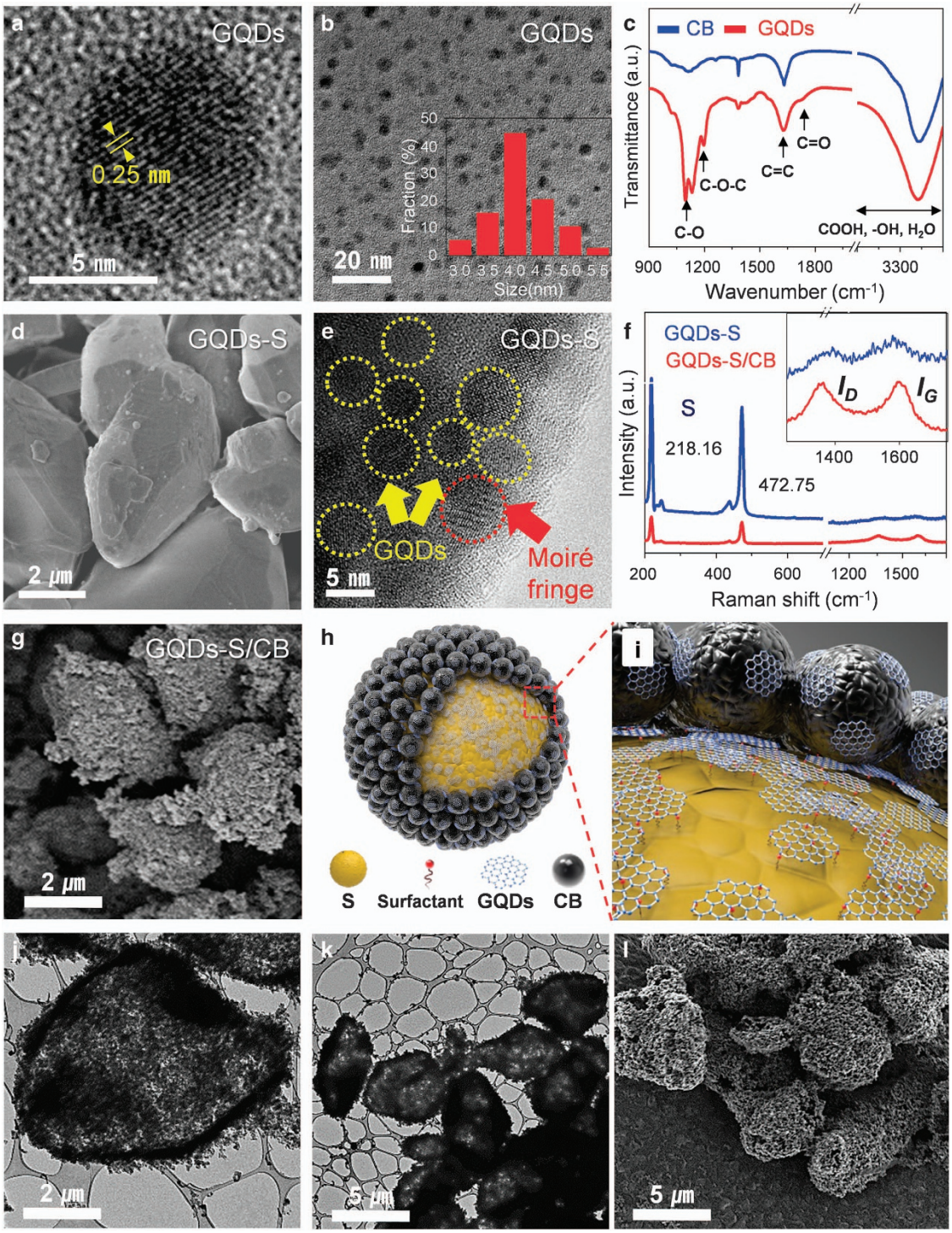

Figure 1 Materials characterization of GQDs-S/CB and S/CB composites. (**a**, **b**) High-resolution TEM images of GQDs; the inset shows a histogram of the GQD size distribution. (**c**) FT-IR spectra of GQDs and CB. The peaks in this figure correspond to the various functional groups in the GQDs and CB. SEM images of (**d**) GQDs-S and (**g**) GQDs-S/CB. (**e**) High-resolution transmission electron microscope (HRTEM) images of the GQDs-S composites and GQD pattern (yellow circle). A Moiré pattern (red circle) is clearly visible in these TEM images, which was created by a superposition of the GQDs and S crystalline lattices. (**f**) Raman spectra of GQDs-S and GQDs-S/CB composites, which show that the GQDs were formed on the sulfur particles. The strong peaks at 218.16 and 472.75 cm^{-1} arise from sulfur, and the D (disorder) and G (graphitic) peaks arise from the GQDs. Schematic diagrams show (**h**) the structure and (**i**) the magnified structure of GQDs-S/CB. (**j**, **k**) HRTEM images, and (**l**) SEM image of the shell structures of GQDs-S/CB after rinsing with a CS_2 solution.

properties of the GQDs. High-resolution transmission electron microscope images were collected to study the morphology of the GQDs (Figure 1a and b). The GQDs were highly crystalline, showing an average size of 4.11 nm (±0.55; the inset of Figure 1b). Oxygen-rich functional groups on the edge of the GQDs, where non-bonding carbons exist, were identified by Fourier transform infrared

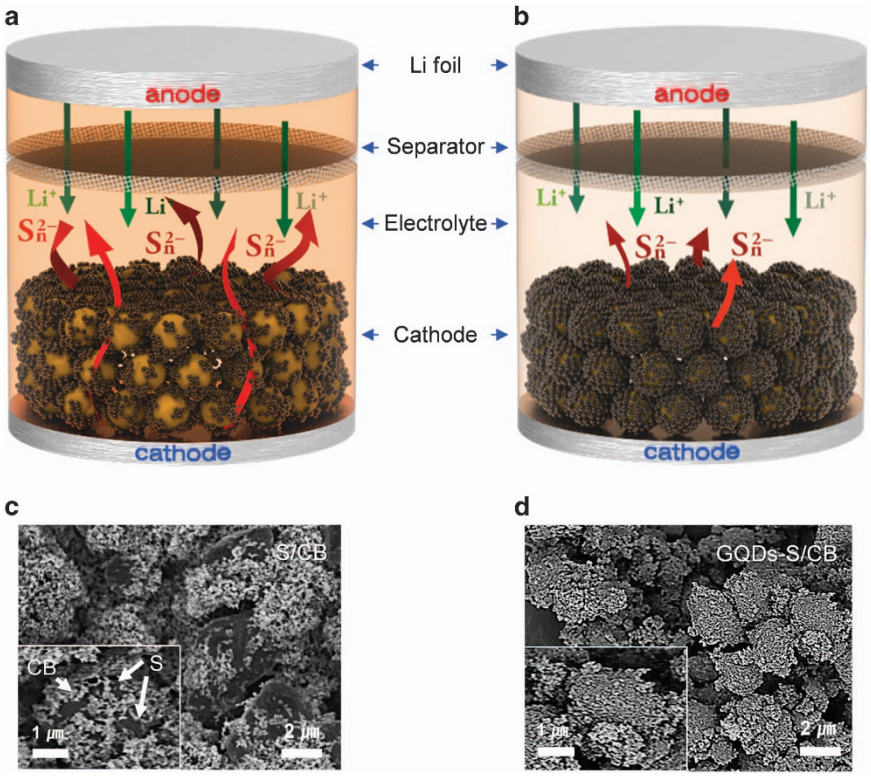

Figure 2 Schematic diagrams and SEM images of S/CB and GQDs-S/CB in a Li–S battery. (**a**, **b**) Schematic configuration of S/CB and GQDs-S/CB employed as a cathode in a Li–S battery. The sulfur (yellow) was wrapped with CB (S/CB) and compactly covered with GQDs and CB (GQDs-S/CB). Polysulfides were dissolved into the solvent and the color changed to orange. (**c**, **d**) SEM images of GQDs-S/CB and S/CB.

spectroscopy (Figure 1c). Strong peaks attributed to the characteristic vibrational modes of oxygen functional groups (-OH at 3434 cm^{-1}, C=O at 1725 cm^{-1}, C–O in 1024–1180 cm^{-1} and C–O–C at 1200 cm^{-1}) could be clearly observed in the spectra of the GQDs, whereas the peak at 1629 cm^{-1} resulted from sp^2-hybridized C=C bonds (in-plane stretching).[27]

Characterization of the GQDs-S composite. The SEM and TEM images in Figure 1d and e show the morphology of the GQDs-S. Sulfur particles measuring several microns were homogeneously coated with GQDs. The uniform distribution of GQDs on the sulfur surface was confirmed by EDS mapping of C, O and S (Supplementary Figure S1). Such a uniform distribution of GQDs could be achieved because of the small size of the GQDs as well as the oxygen functional groups on the particles, which led to electrostatic interactions with sulfur. The graphitic characteristic of GQDs-S was analyzed by Raman spectroscopy (Figure 1f); the peaks for carbon (D and G at 1350 and 1590 cm^{-1}) and sulfur (the four characteristic peaks below 600 cm^{-1}) could be clearly resolved in the spectra.[28,29]

Characterization of the GQDs-S/CB composite. GQDs-S/CB (average particle size of ~50 nm) composite structures were prepared from GQDs-S and CB *via* van der Waals interactions.[12] The SEM image of the GQDs-S/CB composite shown in Figure 1g indicates that CBs were tightly bound to the GQDs-S composites. Scanning TEM-EDS was performed to determine the compositional distribution of C, O and S in the GQDs-S/CB composite, and the results show that C, O and S were homogeneously distributed throughout the composite structure (Supplementary Figure S2). X-ray diffraction analysis of the GQDs-S/CB composite structures reveals high crystallinity and phase purity of sulfur (Supplementary Figure S3a). The composition of GQDs-S/CB was estimated by thermogravimetric analysis (Supplementary Figure S3b) to be 70:20:10 (wt%) S:CB:GQD. XPS, the results of which are shown in Supplementary Figure S4, was performed to analyze the surface of the GQDs-S/CB composite; the results of the quantitative analysis are presented in Supplementary Table S1. The results indicate that a higher C=O intensity (286.7 eV in C 1 s and 530.9 eV in O 1 s) and C–OH (533.0 eV in O 1 s) was observed for GQDs-S/CB than for S/CB because of the oxygen functional group of the GQDs.[30] Moreover, a negligible S 2p signal was detected because the GQDs-S was well covered with CB in the GQDs-S/CB structure (see S 2p in GQDs-S/CB vs S/CB). The schematic illustrations in Figure 1h and i show the GQDs distributed on a sulfur particle, which could strongly bond to CB, leading to a densely packed GQDs-S/CB composite structure. To investigate the structural integrity and mechanical stability of the hierarchal structure, sulfur was dissolved by a CS_2 solution from the GQDs-S/CB composite. Even without sulfur, the structure of the composite was well preserved, as shown in TEM and SEM images (Figure 1j–l).

Schematic Illustration of GQDs-S/CB in a Li–S Battery. The schematic illustration in Figure 2a depicts a conventional Li–S battery, in which the anode and the cathode are made of metallic lithium foil and the composite of sulfur and CB, respectively. The structure of the cathode has a great impact on the irreversible loss of HOPSs during repeated battery operation. In this study, GQDs were introduced into the S/CB cathode, as shown in Figure 2b. The GQDs contained both hydrophobic aromatic and hydrophilic defective regions, which could interact with CBs and sulfur, respectively.[12] SEM images (Figure 2c and d) confirm that the GQDs-S/CB composite electrodes were

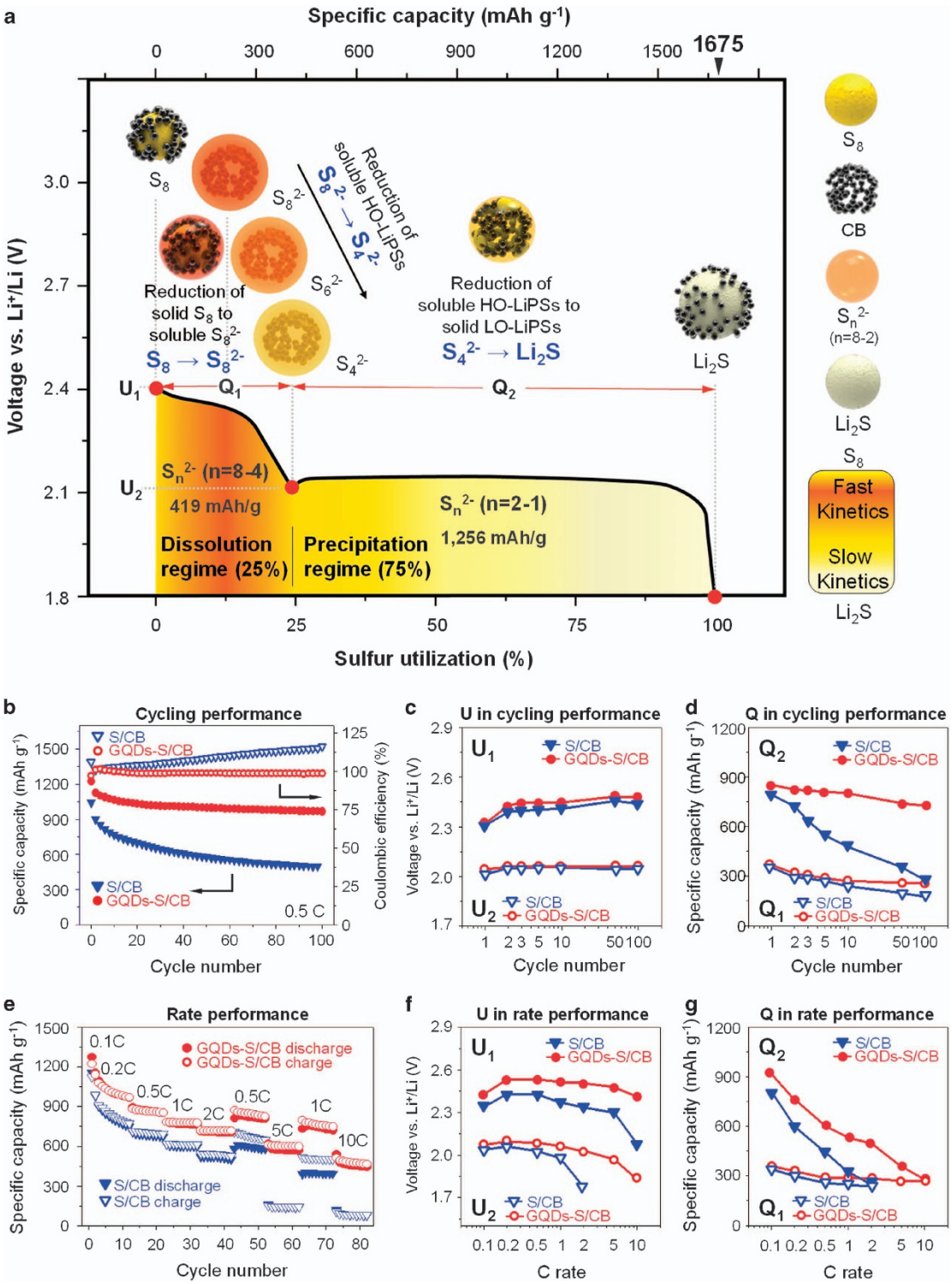

Figure 3 Electrochemical properties of S/CB and GQDs-S/CB electrodes. (**a**) Schematic illustration of the discharge profile of a conventional Li–S battery. HOPSs (S_n^{2-}, n=8–4) and low-order polysulfides (S_n^{2-}, n=2–1) are abbreviated as HO-PSs and LO-PSs, respectively. The onset potential (U) and the capacity (Q) in the dissolution and precipitation regime are noted, which facilitates the analysis of the electrochemical properties of each sample. (**b**) The cycling performance and Coulombic efficiency of both samples at 0.5C over 100 cycles. (**e**) Rate performance of the GQDs-S/CB and S/CB at 0.1C to 10C. (**c**, **f**) Onset potentials as a function of cycle number and (**d**, **g**) capacities as a function of cycle number.

densely packed with CBs, which should have enhanced the electrochemical performance by highly preserving HOPSs in the geometric structure of GQDs-S/CB, whereas the surface of the sulfur particles was partially exposed in the S/CB electrode.

Electrochemical tests for Li–S batteries

Capacity versus voltage profile. The discharge profile in Figure 3a illustrates a schematic model of possible reaction pathways that occur in a conventional Li–S battery. In the upper plateau region at ~ 2.3 V,

elemental sulfur, S_8, is gradually reduced to the soluble sulfide anion (S_8^{2-}). Then, S_8^{2-} is continuously reduced to S_n^{2-} ($n=6$ and 4).[31] These HOPSs (S_n^{2-}, $n=8$-4) are generated and soluble in the electrolyte; thus, the summation of the upper plateau and slope regions between ~2.3 and ~2.1 V can be defined as the dissolution region. Once the composition of S_4^{2-} is reached, HOPSs are further reduced to low-order polysulfides (LOPSs, (S_n^{2-}, $n=2$ and 1)) in the lower plateau region (~2.1 V), whereas HOPSs are soluble in the electrolyte, LOPSs are precipitated as solid phases. Thus, the lower plateau region can be defined as the precipitation region. Finally, Li_2S is formed by the complete reduction of S_8, leading to a theoretical capacity of 1675 mAh g^{-1}. Representative points U_1, U_2, Q_1 and Q_2 are marked in the profile, Figure 3a, where U_1 and U_2 indicate the onset reaction potentials of the dissolved and precipitated species, respectively, whereas Q_1 and Q_2 are the capacities corresponding to the dissolution and precipitation regions, respectively. Q_1 is estimated to be 419 mAh g^{-1} from the reaction S_8 (s)+$4Li^+$+$4e^-$ ↔ $2Li_2S_4$ (l), whereas Q_2 is 1256 mAh g^{-1}, which is achieved by the reduction of HOPSs to LOPSs, $2Li_2S_4$ (l)+$12Li^+$ ↔ $8Li_2S$ (s). In this work, four representative parameters (U_1, U_2, Q_1 and Q_2) and the Q_2/Q_1 ratio (=3) were evaluated to understand the battery performance of GQDs-S/CB composite electrodes.[31]

Cycling performance. The cycling performance of GQDs-S/CB was tested at a 0.5C rate (1C = 1675 mAh g^{-1} assuming the reaction, S_8 +$16Li^+$+$16e^-$ ↔ $8Li_2S$), as shown in Figure 3b. The GQDs-S/CB composites exhibited superior cyclability and stable Coulombic efficiency compared with S/CB. A discharge capacity of ~1000 mAh g^{-1} was achieved even after 100 cycles, whereas S/CB showed a discharge capacity of only 459.6 mAh g^{-1}. Capacity versus voltage profiles at selected cycles are presented in Supplementary Figure S5. The Coulombic efficiency of GQDs-S/CB remained stable at ~100.0% for 100 cycles, whereas that of S/CB continued to increase and reached ~110% at the 100th cycle. The sustained increase in Coulombic efficiency is reported to be attributed to the polysulfide-shuttle phenomenon. Therefore, it is understood that the electrochemically efficient architecture can be provided by GQDs-S/CB, which enables high utilization of active materials, that is, the reversible reaction of sulfur during the discharge process, as confirmed by the Q_2/Q_1 ratio.

The onset potentials (U_1 and U_2) and the capacities (Q_1 and Q_2) as a function of cycle number were derived from the capacity versus voltage profiles and are presented in Figure 3c and d to study the origin of the enhanced cycle performance of the GQDs-S/CB composite. The values of those parameters are also tabulated in Supplementary Tables S2. In the first cycle, U_1 of GQDs-S/CB was 2.33 V, which was slightly higher than that of S/CB, 2.31 V, owing to lower interface resistance. Lower interface resistance is attributed to faster electron transfer kinetics by better carbon coverage in GQDs-S/CB (Figure 3c). The interfacial resistance was further studied by electrochemical impedance spectroscopy, as shown in Supplementary Figure S6.

The radius of the semi-circle (100 kHz–1 Hz) on the Re(Z; ohm) axis is determined by the sum of the interfacial resistance and charge transfer resistance (R_{int}+R_{ct}) based on the equivalent circuit in Supplementary Figure S6a, which indicates that the GQDs-S/CB electrode exhibited a lower complex (interfacial and charge transfer) resistance than the S-CB electrode.[32] The U_2 value of GQDs-S/CB was also slightly higher (Δ30 mV) than that of CB/S, which indicates that HOPSs are more easily reduced to LOPSs. After the first cycle, a slight increase in U_1 and U_2 was observed for both electrodes because of the decrease in the overpotential resulting from the rearrangement of micron-sized sulfur.[33] The U_1 and U_2 values of GQDs-S/CB were higher than those of S/CB over 100 cycles, which confirms that the GQDs-S/CB composite has relatively low resistance to the discharge process at each cycle. In contrast, Q_1 and Q_2 exhibit quite different behavior between GQDs-S/CB and S/CB, as shown in Figure 3d. For the first cycle, higher Q_1 and Q_2 value were observed in GQDs-S/CB (Q_1 = 370.90 mAh g^{-1} and Q_2 = 853.24 mAh g^{-1}) compared with those observed in S/CB (Q_1 = 354.86 mAh g^{-1} and Q_2 = 793.35 mAh g^{-1}) because of the more efficient utilization of active materials by the introduction of GQDs. However, the Q_2/Q_1 ratios were still low in both the GQDs-S/CB (Q_2/Q_1 = 2.30) and S/CB (Q_2/Q_1 = 2.24) samples. Such a low Q_2/Q_1 ratio for the first cycle can be ascribed to the irreversible initial loss of HOPSs and the inefficient precipitation of LOPSs. Afterward, the Q_1 and Q_2 values gradually decreased with extended cycling in S/CB. Notably, the Q_1 values showed relatively slow decay, but severe fading of Q_2 was observed, which indicates that the precipitation reaction was impeded by the loss of active sites. In contrast, the Q_1 and Q_2 values were maintained for GQDs-S/CB even after 100 cycles through a minimized loss of active species and preservation of active sites to facilitate reactions. The Q_2/Q_1 ratios in GQDs-S/CB were determined to be 2.94 and 2.81 at the 10th cycle and the 100th cycle, respectively, which are close to the theoretical value (=3), whereas the Q_2/Q_1 ratios of S/CB were 1.96 and 1.55 at the 10th and 100th cycles, respectively. Such high Q_2/Q_1 ratios strongly indicate that the redox reaction between S_8 and Li_2S can occur very reversibly owing to the highly efficient electrode structure driven by the GQDs. The GQDs can aid in capturing the HOPSs during the electrochemical reaction, which will be discussed in detail later. In addition, the results of the electrochemical impedance spectroscopy study (Supplementary Figure S6b and c) and associated discussion supporting polysulfide (PS) capture by GQDs can are provided in the supplementary section. Even though an electrode with high sulfur loading was prepared (~2.2 mg cm^{-2}), GQDs-S/CB showed superior cycle performance (~950 mAh g^{-1}) compared with that of S/CB (~280 mAh g^{-1}) (Supplementary Figure S7), which indicates higher cycle performance compared with that reported in previous studies of carbon/sulfur composites (Supplementary Table S4).

Rate capability. The rate capabilities of GQDs-S/CB and S/CB were tested from 0.1C to 10C and are presented in Figure 3e (see Supplementary Figure S8 for the capacity versus voltage profiles at the different rates). The GQDs-S/CB showed excellent rate capabilities compared with those of S/CB. Supplementary Figure S9 shows that a high discharge capacity of 540.17 mAh g^{-1} at 10C could be attained (42% versus the discharge capacity at C/10) in GQDs-S/CB. In contrast, a discharge capacity of only 120.35 mAh g^{-1} could be achieved at 10C (10% versus that at C/10) in S/CB. This rate performance, even at the 10C rate, demonstrates the superior properties of the composite compared with those reported in previous studies in Supplementary Figure S10. To study the origin of such high rate capabilities in the GQDs-S/CB electrodes, the evolution of four parameters with the rate were investigated. The U_1 and U_2 values were derived from the rate capability tests, as shown in Figure 3f. The GQDs-S/CB electrode showed slightly higher U_1 and U_2 values than those of S/CB at a relatively low rate (<0.2 C). However, the U_1 and U_2 values of the S/CB electrodes decreased significantly at a rate above 0.5C, whereas the U_1 and U_2 values of the GQDs-S/CB electrodes remained more stable. The higher U_1 and U_2 values in the GQDs-S/CB electrode confirm that the GQDs increase the electrical conductivity of the material as well as provide an electrochemically

efficient structure, whereby overpotentials that are required to initiate the dissolution (U_1) and precipitation (U_2) reactions are decreased. It should be noted that the tendencies observed for U_1 and U_2 are similar because these values are related to the overpotential in the reduction of S_8 and HOPSs, respectively. In contrast, different behaviors were observed for Q_1 and Q_2, particularly under the highest current density, as shown in Figure 3g. The reaction kinetics for the formation of HOPSs is fast; thus, Q_1 is less affected by high current density.[33] However, a significant decrease in Q_2 was observed at higher current density, which is attributed to the slow reduction due to the low electrical conductivity of LOPSs or limited reaction sites. The Q_2/Q_1 ratios in S/CB were 2.36 and 1.27, at 0.1C and 2C, respectively, whereas higher Q_2/Q_1 ratios, 2.55 (at 0.1 C) and 1.75 (at 2 C), were achieved in GQDs-S/CB, which indicates that efficient utilization of sulfur occurred through the facile charge transfer and the high density of reaction sites.

Post-mortem analysis

Morphological evolution. SEM images of the anodes and cathodes (Supplementary Figures S11 and S12, respectively) were obtained from the GQDs-S/CB and S/CB electrodes after 20 cycles. Because of the formation of a thick solid electrolyte interphase (SEI) layer, the SEM images of the cathodes in Supplementary Figure S11 show flattened morphologies. Interestingly, homogenous surfaces could be observed in GQDs-S/CB, whereas segregation of sulfur was observed in the CB/S electrode. This morphological difference was driven by the structural integrity of GQDs-S/CB. Because GQDs-S/CB electrodes could provide stable reaction sites during repeated cycling and preserve HOPSs in the vicinity of the electrode, the morphological change could be minimized. Moreover, continuous dissolution and precipitation of sulfur led to the significant change in the electrode morphology of CB/S, ultimately resulting in the segregation of sulfur on the surface of the electrode. Such loss of sulfur from the cathode was also observed in the anode. A clean surface was observed on the GQDs-S/CB anode, whereas the CB/S anode contained S and Li_2S particles on the surface, as confirmed by EDS and Raman spectroscopy (Supplementary Figure S12). As previously mentioned, these sulfur and Li_2S deposits resulted from the active materials lost from the cathode side during repeated cycling.

Surface modifications. To study the detailed mechanism through which the GQDs imparted high performance, the chemical bonding states of the S/CB and GQDs-S/CB electrodes harvested from the various states were characterized by XPS (Figure 4a–c). The C 1 s spectra of the as-prepared electrodes (Figure 4a) show peaks at 283.8 eV and 284.5 eV attributed to sp^2 and sp^3 hybridized carbons, respectively, whereas the peak at 285.3 eV corresponds to C–S bonding.[34,35] The peak at 286.2 eV is assigned to C–OH bonding, which is more intense in GQDs-S/CB than in S/CB because the GQDs have a high density of -OH surface functional groups. The two peaks that correspond to carbonyl and carboxyl groups are located at 287.0 and 289.0 eV, respectively. The C 1 s spectra of the S/CB electrode harvested from both charged and discharged stages after the 20th cycle (Figure 4b and c) show a slight decrease and an increase in the intensity of the C–OH (286.3 eV) and C–S (285.3 eV) peaks, respectively. Although the GQDs-S/CB electrode showed a noticeable decrease in the hydroxyl peak (286.2 eV), a C–S peak (285.4 eV) became prominent in both the charged and discharged states after 20 cycles. The change in the bonding nature indicates that hydroxyl groups in the GQDs facilitated the formation of C–S bonds during cycling. The C–S bonds generated in the GQDs-S/CB electrodes indicate that the GQDs exhibited sulfiphilic properties, enabling sulfur to be preserved in the vicinity of GQDs. Thus, the Q_2/Q_1 ratio was stable at ~2.9 even after 100 cycles. The C–F_2 peak at ~291.0 eV and the C-F_3 peak at ~293.0 eV originated from the binder (polyvinylidene fluoride) and electrolyte salt (lithium bis(trifluoromethane) sulfonimide), respectively.[36] The S 2p spectra of the electrodes harvested after 20 cycles also support the formation of C–S bonding (Supplementary Figure S13). The C–S bonding peaks at 162.6 eV are observed in both the S/CB and GQDs-S/CB electrodes. However, the intensity of C–S bonding in the GQDs-S/CB electrode was higher than

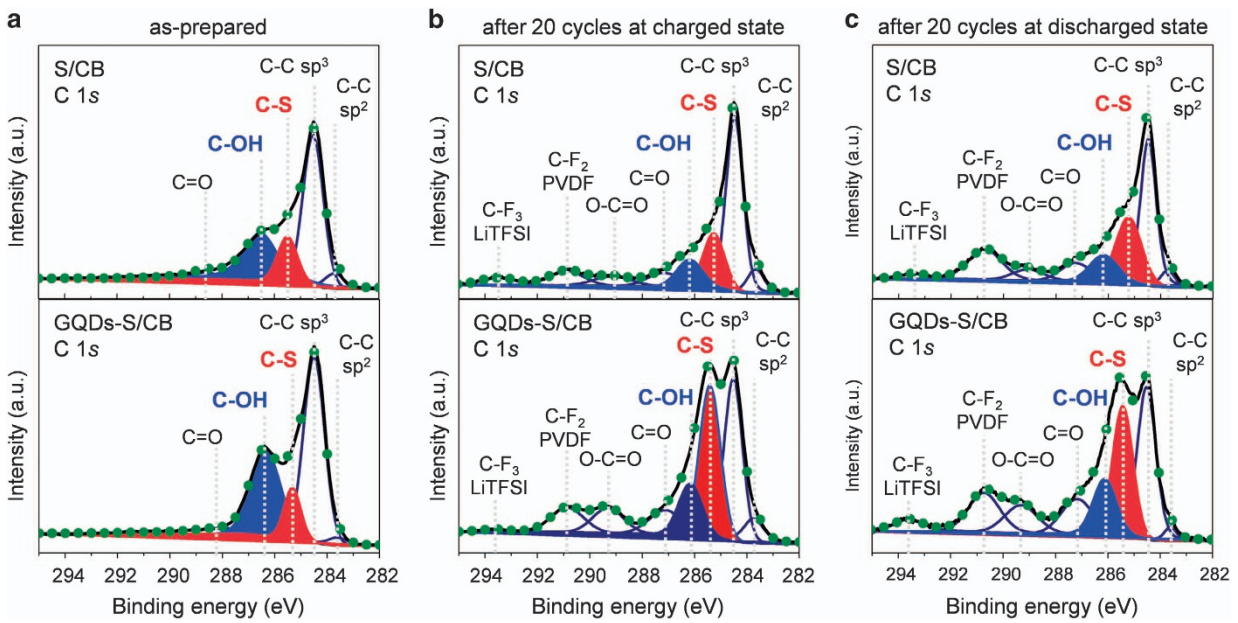

Figure 4 Post-mortem analysis of high-resolution X-ray photoelectron spectra (XPS). C 1 s high-resolution XPS spectra of the S/CB and GQDs-S/CB electrodes (**a**) before cycling and after 20 cycles in the (**b**) charged and (**c**) discharged state. Each spectrum was fitted with functions corresponding to different valencies of carbon and sulfur (navy solid line), and the sum of those fitted curves (green dots) is consistent with the raw data (black solid line).

that in the S/CB electrode.[29] The S–S bonding at ~ 164.0 eV is ascribed to the crystalline sulfur in the electrode.[30] The S–S peak intensity of GQDs-S/CB was higher than that of S/CB because more elemental sulfur was reduced on the electrode. Adsorption processes prevented the irreversible loss of the active material into the electrolyte by the formation of nano-sized sulfur that bonded favorably to the GQDs, as discussed later. The peaks at 167.0 eV and ~ 170.0 eV are attributed to sulfate, SO_2, from LiTFSI and oxidized polysulfide species, SO_3, respectively.[36]

Theoretical modeling

DFT calculations were performed to clarify the formation of C–S bonding between the GQDs and sulfur species. The calculation is based on the following reaction:

$$\text{coronene_OH} + S_n^{2-} \rightarrow (\text{coronene_S}_n)^- + OH^- \quad (n = 1, 2, 4, 6, 8)$$

This model was used to represent the terminal edges of the GQDs, and we attached a hydroxyl group (–OH) to one of the edges of the carbon atoms, 'coronene_OH'.[37] A coronene is a polycyclic aromatic hydrocarbon comprising six peri-fused benzene rings with the chemical formula $C_{24}H_{12}$. Moreover, the coronene model is composed of small sp^2 clusters and is isolated by sp^3 carbon, which is close to individual GQDs without oxygen functional groups, and it has been previously employed as a reduced model of graphene for quantum calculations in lithium–sulfur battery studies.[37,38] The relative energies calculated by DFT for the reactants and products indicate that replacing the terminal hydroxyl group by a sulfur dianion results in a lower energy state. The relative energies are shown in Figure 5, where it is clear that the energies of the product decrease when sulfur dianions are replaced with the terminal hydroxyl group. The lower energy of the products (S_n^{2-}, $n = 1$, 2, 4 and 6) can provide a driving force for the reaction, thus making the formation of C–S bonds favorable. However, the small sulfur dianions normally exist in the form of a solid crystal combined with lithium cations such that Li_2S that cannot easily participate in C–S bonding.[39] Furthermore, large sulfur dianion chains ($n > 6$) tend to disassemble into smaller chains.[39] Thus, it is speculated that the major participants in the reaction are S_2^{2-}, S_4^{2-} and S_6^{2-} ions. In addition, the same DFT calculation was performed for carboxyl group-terminated coronene (coronene_-COOH) (Supplementary Figure S14), which produced results similar to those obtained for the coronene_OH group. Our results highlight the crucial role of the formation of C–S bonds through terminal oxygen functional groups present on the edge of GQDs.

Study of C–S bonding based on electrochemical cells using catholyte

Intrinsic surface interactions at the interface between GQDs and CB were studied by electrochemical cycling with Li_2S_8 catholyte. GQDs/CB and CB electrodes without sulfur were prepared and electrochemically cycled in Li_2S_8 catholyte. The cycle retention of GQDs/CB exceeded 90% over 100 cycles, whereas CB exhibited $<80\%$ capacity retention (Supplementary Figure S15c). After cycling

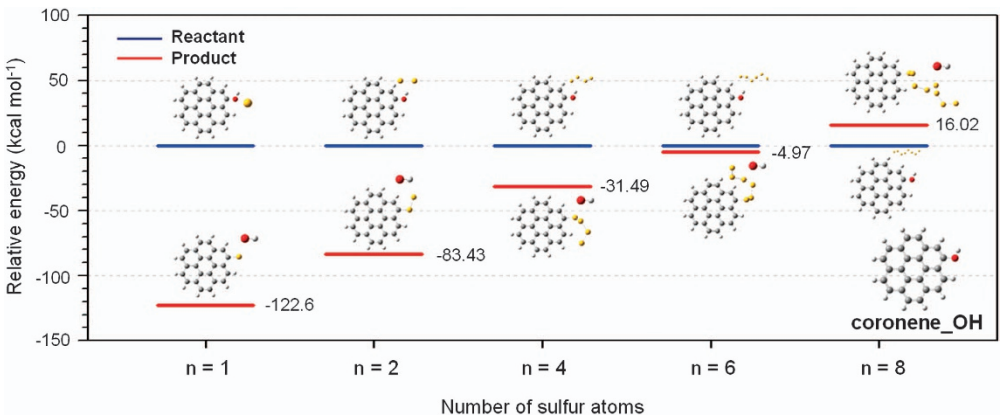

Figure 5 The relative energies for the reactants and products in the binding of polysulfides to GQDs. A plot of the relative energies for the reactants and products in the binding of polysulfides to GQDs versus the sulfur chain length. The functional groups on GQDs enhanced the binding of polysulfides to the carbon because of the substitution of S_n^{2-} for –OH (C–OH). Yellow, red, white and gray represent S, O, H and C atoms, respectively.

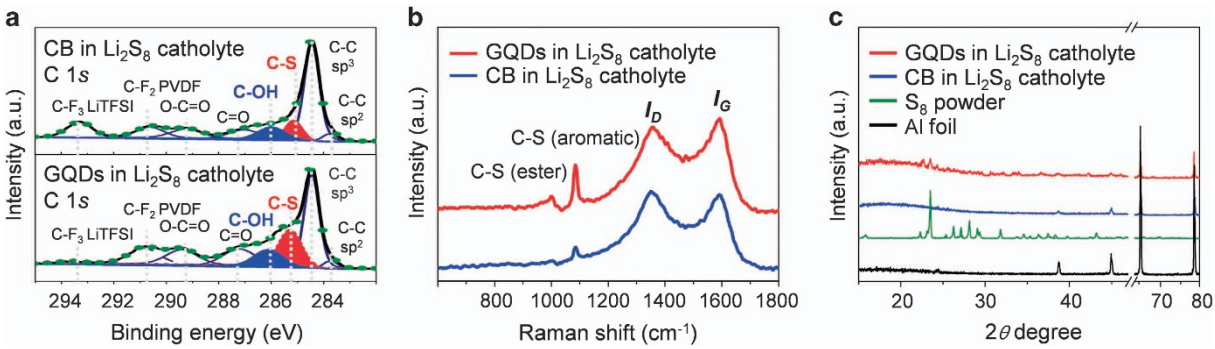

Figure 6 Post-mortem analysis of GQDs and CB electrode in Li_2S_8 catholyte. (**a**) C 1 s high-resolution XPS spectra, (**b**) Raman spectra and (**c**) X-ray diffraction (XRD) spectra of CB and GQDs electrodes in Li_2S_8 catholyte after 20 cycles in the charged state. Raman spectra showing C–S (aromatic and ester) bond formation within the samples.

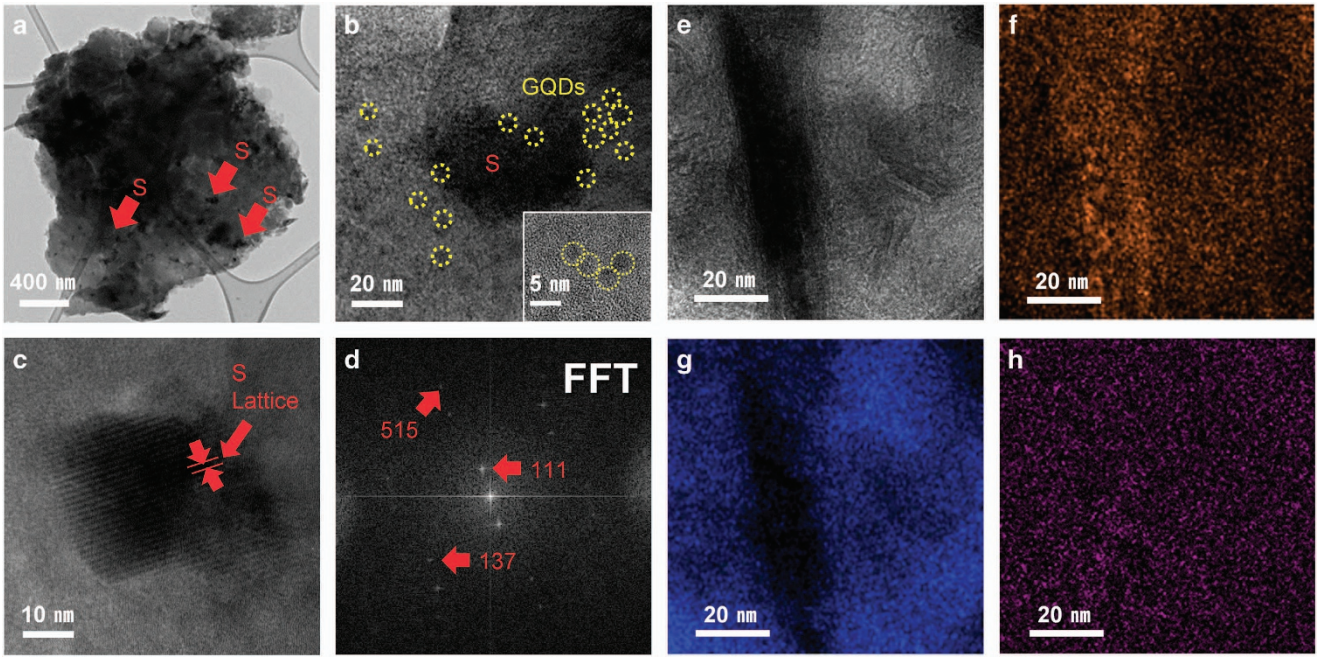

Figure 7 TEM and Scanning TEM images of nano-sized sulfur on GQDs electrode in Li_2S_8 catholyte after 20 cycles in the charged state. (**a**) Low- and high-magnification images of nano-sized sulfur in GQD materials. The lump represents the GQDs electrode with nano-sized sulfur, and the small dark particles are nano-sized sulfur. (**b**) GQDs covered on nano-sized sulfur particle. (**c**) High-resolution transmission electron microscope (HRTEM) image showing the lattice fringes of the nano-sized sulfur and the GQDs. (**d**) The fast Fourier transform (FFT) of the original HRTEM image is **c** in the center of the filtered image. The two bright spots represent sulfur particles, and the other spot indicates the GQDs lattice plane. (**e**) STEM image of GQDs electrode in the catholyte after cycling. Electron energy loss spectroscopy (EELS) maps of (**f**) sulfur, (**g**) carbon and (**h**) oxygen in the GQDs/CB electrode.

the GQDs/CB electrode, the C 1 s and S 2p XPS spectra (Figure 6a, Supplementary Figure S15a and b) showed higher S–S and C–S peaks compared with those exhibited by CB. Furthermore, Raman peaks for C–S aromatic bonding at 1086 cm^{-1} and for C–S esteric bonds at 997 cm^{-1} were more intense for the GQDs/CB electrodes.[40] The carbon peaks at 1590 cm^{-1} and 1350 cm^{-1} were assigned to the G and the D bands of carbon, respectively (Figure 6b). X-ray diffraction of the GQDs/CB electrodes also confirmed the formation of nano-sized crystalline sulfur (Figure 6c), which strongly indicates that PSs were adsorbed on the oxygen functional groups of GQDs.

The formation of nano-sized crystalline sulfur was also observed by TEM analysis. After 20 electrochemical cycles with Li_2S_8 catholyte, only a small number of sulfur particles were observed on the CB electrode (Supplementary Figure S16), whereas many nano-sized sulfur particles can be observed on the GQD electrode in Figure 7a–d. Nano-sized sulfur particles were covered with GQDs, which was confirmed by lattice fringes corresponding to (111) planes. In addition, the indices of bright spots on the fast Fourier transform image indicate that sulfur was single-crystalline and crystallized in the orthorhombic structure of the alpha phase (JCPDS, No. 08-0247).[41] The broad ring patterns in the fast Fourier transform image indicate the presence of multiple GQDs with different orientations in Supplementary Figure S17. The TEM-electron energy loss spectroscopy and SEM-EDS analyses of the GQDs also indicate that nano-sized sulfur particles were adsorbed onto the GQDs (Supplementary Figure S16a–d, i–l). In contrast, the CB electrode contained a low sulfur density (Supplementary Figure S16e–h, m–p). This observation suggests that the GQDs exhibited sulfiphilic properties, leading to the preferred nucleation of sulfur on the GQDs. Furthermore, sulfur could easily be adsorbed/desorbed on the GQDs, as predicted by the aforementioned DFT calculation.

CONCLUSIONS

We designed GQDs-S/CB composites as high-performance cathode materials for the first time in Li–S batteries. The nano-sized GQDs induce a tightly packed structure *via* charge interaction with S and CB, resulting in enhanced conductivity by shortened electron conduction paths. Furthermore, C–S bonding is generated *in situ* during battery operation, which originates from the oxygen-rich functional group at the edge of the GQDs. Thus, the loss of active materials into the electrolyte is minimized. The adsorption of nano-sized sulfur particles onto the GQD interfaces by C–S bonding was predicted by DFT calculation and experimentally confirmed by various microscopic and spectroscopic analyses. The GQDs-S/CB composites significantly improve cycling and rate performances, and their electrochemical behavior could be understood by an in-depth analysis of discharge profiles. We believe that our results provide a new avenue for researchers to tailor the oxygen-rich functional groups of nano-sized carbon for application in Li–S batteries as well as various energy storage devices.

CONFLICT OF INTEREST

The authors declare no conflict of interest.

ACKNOWLEDGEMENTS

Y.-E.S. acknowledges financial support from the Institute for Basic Science (Grant No. IBS-R006-G1), Republic of Korea. B.H.H. acknowledges financial support from the Basic Science Research Program (2011-0017587) and the Global Research Lab (GRL) Program (2011-0021972) through the National Research Foundation of Korea funded by the Ministry of Science, ICT & Future, Korea. C.K. and J.C. were supported as part of the Joint Center for Energy Storage Research (JCESR), an Energy Innovation Hub funded by the US Department of Energy, Office of Science, Basic Energy Sciences. X-ray

diffraction analyses were supported by the Pohang Accelerator Laboratory (beamline 5A) and Korea I.T.S. Laboratory, Republic of Korea.

Author contributions: Y.-E.S. and B.H.H. conceived and supervised the project. J.P., J.M. and C.K. led the project. Y.-E.S., B.H.H., J.P., J.M. and C.K. wrote the manuscript, performed the laboratory experiments and analyzed the results. J.H.K. and J.P. assisted with materials analysis. E.L. and J.H. contributed to theoretical modeling. K.J.L. and S.-H.Y. assisted with electrochemical analysis. J.-H.S. and J.L. contributed to surface analysis. S.-P.C. and T.N. carried out TEM imaging. J.C., C.K. and J.P. prepared the manuscript, which incorporates critical input from all authors.

1 Goodenough, J. B. & Park, K.-S. The Li-ion rechargeable battery: a perspective. *J. Am. Chem. Soc.* **135**, 1167–1176 (2013).
2 Cabana, J., Monconduit, L., Larcher, D. & Palacín, M. R. Beyond intercalation-based Li-ion batteries: the state of the art and challenges of electrode materials reacting through conversion reactions. *Adv. Mater.* **22**, E170–E192 (2010).
3 Manthiram, A., Fu, Y. & Su, Y.-S. Challenges and prospects of lithium-sulphur batteries. *Acc. Chem. Res.* **46**, 1125–1134 (2013).
4 Chung, W. J., Griebel, J. J., Kim, E T., Yoon, H., Simmonds, A. G., Ji, H. J., Dirlam, P. T., Glass, R. S., Wie, J. J., Nguyen, N. A., Guralnick, B. W., Park, J., Somogyi, A., Theato, P., Mackay, M. E., Sung, Y. E., Char, K. & Pyun, J. The use of elemental sulphur as an alternative feedstock for polymeric materials. *Nat. Chem.* **5**, 518–524 (2013).
5 Bruce, P. G., Freunberger, S. A., Hardwick, L. J. & Tarascon, J.-M. Li-O_2 and Li-S batteries with high energy storage. *Nat. Mater.* **11**, 19–29 (2012).
6 Choi, N.-S., Chen, Z., Freunberger, S. A., Ji, X., Sun, Y.-K., Amine, K., Yushin, G., Nazar, L. F., Cho, J. & Bruce, P. G. Challenges facing lithium batteries and electrical double-layer capacitors capacitors. *Angew. Chem. Int. Ed.* **51**, 9994–10024 (2012).
7 Ji, L., Aloni, S., Wang, L., Cairns, E. J. & Zhang, U. Porous carbon nanofiber-sulphur composite electrodes for lithium/sulphur cells. *Energy Environ. Sci.* **4**, 5053–5059 (2011).
8 Zhou, G., Pei, S., Li, L., Wang, D.-W., Wang, S., Huang, K., Yin, L. C., Li, F. & Cheng, H. M. A graphene-pure-sulfur sandwich structure for ultrafast, long-life lithium-sulfur batteries. *Adv. Mater.* **26**, 625–634 (2014).
9 Ji, X., Lee, K. T. & Nazar, L. F. A Highly ordered nanostructured carbon-sulphur cathode for lithium-sulphur batteries. *Nat. Mater.* **8**, 500–506 (2009).
10 Xin, S., Gu, L., Zhao, N.-H., Yin, Y.-X., Zhou, L.-J., Guo, Y.-G. & Wan, L. J. Smaller sulphur molecules promise better lithium-sulphur batteries. *J. Am. Chem. Soc.* **134**, 18510–18513 (2012).
11 Guo, J., Xu, Y. & Wang, C. Sulphur-impregnated disordered carbon nanotubes cathode for lithium sulphur batteries. *Nano Lett.* **11**, 4288–4294 (2011).
12 Wang, H., Yang, Y., Liang, Y., Robinson, J. T., Li, Y., Jackson, A., Cui, Y. & Dai, H. Graphene–wrapped sulphur particles as a rechargeable lithium-sulphur battery cathode material with high capacity and cycling stability. *Nano Lett.* **11**, 2644–2647 (2011).
13 Ji, L., Rao, M., Zheng, H., Zhang, L., Li, Y., Duan, W., Guo, J., Cairns, E. J. & Zhang, Y. Graphene oxide as a sulphur immobilizer in high performance lithium/sulphur cells. *J. Am. Chem. Soc.* **133**, 18522–18525 (2011).
14 Zu, C. & Manthiram, A. Hydroxylated graphene-sulphur nanocomposites for high-rate lithium-sulphur batteries. *Adv. Energy Mater.* **3**, 1008–1012 (2013).
15 Evers, S. & Nazar, L. F. Graphene-enveloped sulphur in a one pot reaction: a cathode with good coulombic efficiency and high practical sulphur content. *Chem. Commun.* **48**, 1233–1235 (2012).
16 Moon, J., Park, J., Jeon, C., Lee, J., Jo, I., Yu, S., Cho, S. P., Sung, Y. E. & Hong, B. H. An electrochemical approach to graphene oxide coated sulphur for long cycle life. *Nanoscale* **7**, 13249–13255 (2015).
17 Fu, Y. & Manthiram, A. Orthorhombic bipyramidal sulphur coated with polypyrrole nanolayers as a cathode material for lithium-sulfur batteries. *J. Phys. Chem. C* **116**, 8910–8915 (2012).
18 Peng, J., Gao, W., Gupta, B. K., Liu, Z., Romero-Aburto, R., Ge, L., Song, L., Alemany, L. B., Zhan, X., Gao, G., Vithayathil, S. A., Kaipparettu, B. A., Marti, A. A., Hayashi, T., Zhu, J. J. & Ajayan, P. M. Graphene quantum dots derived from carbon fibers. *Nano Lett.* **12**, 844–846 (2012).
19 Ye, R., Xiang, C., Lin, J., Peng, Z., Huang, K., Yan, Z., Cook, N. P., Samuel, E. L., Hwang, C. C., Ruan, G., Ceriotti, G., Raji, A. R, Martí, A. A. & Tour, J. M. Coal as an abundant source of graphene quantum dots. *Nat. Commun.* **4**, 2943 (2013).
20 Ritter, K. A. & Lyding, J. W. The influence of edge structure on the electronic properties of graphene quantum dots and nanoribbons. *Nat. Mater.* **8**, 235–242 (2009).
21 Pan, D., Zhang, J., Li, Z. & Wu, M. Hydrothermal route for cutting graphene sheets into blue-luminescent graphene quantum dots. *Adv. Mater.* **22**, 734–738 (2010).
22 Konstantatos, G., Badioli, M., Gaudreau, L., Osmond, J., Bernechea, M., Arquer, F. P. G., Gatti, F. & Koppens, F. H. Hybrid graphene-quantum dot phototransistors with ultrahigh gain. *Nat. Nanotechnol.* **7**, 363–368 (2012).
23 Chao, D., Zhu, C., Xia, X., Liu, J., Zhang, X., Wang, J., Liang, P., Lin, J., Zhang, H., Shen, Z. X. & Fan, H. J. Graphene quantum dots coated VO_2 arrays for highly durable electrodes for Li and Na ion batteries. *Nano Lett.* **15**, 565–573 (2015).
24 Zhu, C., Chao, D., Sun, J., Bacho, L. M., Fan, Z., Ng, C. F., Xia, X., Huang, H., Zhang, H., Shen, Z. X., Ding, G. & Fan, H. J. Enhanced lithium storage performance of CuO nanowires by coating of graphene quantum dots. *Adv. Mater. Interfaces* **2**, 1400499 (2015).
25 Stephens, P. J., Devlin, F. J., Chabalowski, C. F. & Frisch, M. J. Ab Initio calculation of vibrational absorption and circular dichroism spectra using density functional force fields. *J. Phys. Chem.* **98**, 11623–11627 (1994).
26 Frisch, M. J., Trucks, G. W., Schlegel, H. B., Scuseria, G. E., Robb, M. A., Cheeseman, J. R., Scalmani, G., Barone, V., Mennucci, B., Petersson, G. A., Nakatsuji, H., Caricato, M., Li, X., Hratchian, H. P., Izmaylov, A. F., Bloino, J., Zheng, G., Sonnenberg, J. L., Hada, M., Ehara, M., Toyota, K., Fukuda, R., Hasegawa, J., Ishida, M., Nakajima, T., Honda, Y., Kitao, O., Nakai, H., Vreven, T., Montgomery, J. A., Jr., Peralta, J. E., Ogliaro, F., Bearpark, M., Heyd, J. J., Brothers, E., Kudin, K. N., Staroverov, V. N., Kobayashi, R., Normand, J., Raghavachari, K., Rendell, A., Burant, J. C., Iyengar, S. S., Tomasi, J., Cossi, M., Rega, N., Millam, J. M., Klene, M., Knox, J. E., Cross, J. B., Bakken, V., Adamo, C., Jaramillo, J., Gomperts, R., Stratmann, R. E., Yazyev, O., Austin, A. J., Cammi, R., Pomelli, C., Ochterski, J. W., Martin, R. L., Morokuma, K., Zakrzewski, V. G., Voth, G. A., Salvador, P., Dannenberg, J. J., Dapprich, S., Daniels, A. D., Farkas, Ö., Foresman, J. B., Ortiz, J. V., Cioslowski, J. & Fox, D. J. *Gaussian 09* (Gaussian, Inc.: Wallingford CT, 2009).
27 Acik, M., Lee, G., Mattevi, C., Pirkle, A., Wallace, R. M., Chhowalla, M., Cho, K. & Chabal, Y. The role of oxygen during thermal reduction of graphene oxide studied by infrared absorption spectroscopy. *J. Phys. Chem. C* **115**, 19761–19781 (2011).
28 Gokus, T., Nair, R. R., Bonetti, A., Bohmler, M., Lombardo, A., Noboselov, K. S., Geim, A. K., Ferrari, A. C. & Hartschuh, A. Making graphene luminescent by oxygen plasma treatment. *ACS Nano* **3**, 3963–3968 (2009).
29 Yeon, J.-T., Jang, J.-Y., Han, J.-G., Cho, J., Lee, K. T. & Choi, N.-S. Raman spectroscopy and X-ray diffraction studies of sulphur composite electrodes during discharge and charge. *J. Electrochem. Soc.* **159**, A1308–A1314 (2012).
30 Moulder, J. F., Stickle, W. F., Sobol, P. E. & Bomben, K. D. *Handbook of X-ray Photoelectron*, (Spectroscopy, Physical Electronics, Inc., 1995).
31 Su, Y.-S., Fu, Y., Cochell, T. & Manthiram, A. A strategic approach to recharging lithium-sulphur batteries for long cycle life. *Nat. Commun.* **4**, 2985–2992 (2013).
32 Deng, Z., Zhang, Z., Lai, Y., Liu, J., Li, J. & Liu, Y. Electrochemical impedance spectroscopy study of a lithium/sulphur battery: modelling and analysis of capacity fading. *J. Electrochem. Soc.* **4**, A553–A558 (2013).
33 Bruckner, J., Soren, T., Grossmann, H. T., Dorfler, S., Althues, H. & Kaskel, S. Lithium sulphur batteries: influence of C-rate, amount of electrolyte and sulphur loading on cycle performance. *J. Power Sources* **268**, 82–87 (2014).
34 Kaciulis, S. Spectroscopy of carbon: from diamond to nitride films. *Surf. Interface Anal.* **44**, 1155–1161 (2012).
35 Kummer, K., Vyalikh, D. V., Gavrila, G., Kade, A., Weigel-Jech, M., Mertig, M. & Molodtsov, S. L. High-resolution photoelectron spectroscopy of self-assembled mercaptohexanol monolayers on gold surfaces. *J. Electron Spectrosc. Relat. Phenom.* **163**, 59–64 (2008).
36 Song, J., Lee, S. J., Kim, Y., Kim, S.-S., Lee, K. T. & Choi, N.-S. Thermal reactions of lithiated and delithiated sulphur electrodes in lithium-sulfur batteries. *ECS Electrochem. Lett.* **3**, A26–A29 (2014).
37 Song, J., Xu, T., Gordin, M. L., Zhu, P., Lv, D., Jiang, Y.-B., Duan, Y. & Wang, D. Nitrogen-doped mesoporous carbon promoted chemical adsorption of sulphur and fabrication of high-areal-capacity sulphur cathode with exceptional cycling stability for lithium-sulphur batteries. *Adv. Funct. Mater.* **24**, 1243–1250 (2014).
38 Sk, M. A., Ananthanarayanan, A., Huang, L., Lim, K. H. & Chen, P. Revealing the tunable photoluminescence properties of graphene quantum dots. *J. Mater. Chem. C* **2**, 6954–6960 (2014).
39 Berghof, V., Sommerfeld, T. & Cederbaum, L. S. Sulfur cluster dianions. *J. Phys. Chem. A* **102**, 5100–5105 (1998).
40 Socrates, G. *Infrared and Raman characteristic group frequencies tables and charts: Sulphur and Selenium compounds*. 3rd edn Ch.16 (John Wiley & Sons Ltd, 2001).
41 Abrahams, S. C. The crystal and molecular structure of orthorhombic sulphur. *Acta Crystallogr.* **8**, 661–671 (1955).

This work is licensed under a Creative Commons Attribution 4.0 International License. The images or other third party material in this article are included in the article's Creative Commons license, unless indicated otherwise in the credit line; if the material is not included under the Creative Commons license, users will need to obtain permission from the license holder to reproduce the material. To view a copy of this license, visit http://creativecommons.org/licenses/by/4.0/

Supplementary Information accompanies the paper on the NPG Asia Materials website (http://www.nature.com/am)